Elucidating Pore and Surface Features of Soot Nanoparticles using Molecular Dynamics Simulations

Khaled Mosharraf Mukut[a], Eirini Goudeli[b], Georgios A. Kelesidis[c], Somesh P. Roy[a,*]

[a] *Department of Mechanical Engineering, Marquette University, Milwaukee, Wisconsin, U.S.A.*

[b] *Department of Chemical Engineering, University of Melbourne, Victoria, Australia*

[c] *Faculty of Aerospace Engineering, Delft University of Technology, Delft, The Netherlands*

Abstract

Understanding the surface and pore features of soot nanoparticles is important for predicting their behavior in combustion environments and atmospheric processes. Here, we present a novel computational framework combining reactive molecular dynamics simulations with detailed atomistic analysis to characterize the morphology of over 2000 incipient soot particles formed from acetylene pyrolysis at 1350-1800 K. The surface and pore features of these nanoparticles are explored directly using three-dimensional atomic surface mesh for the first time. The nanoparticles are found to have a highly irregular shape, with an average sphericity of 0.57 and a surface fractal dimension (D_S) of approximately 2.22. The particles exhibit sig-

*Corresponding author: somesh.roy@marquette.edu

nificant internal porosity ($\Phi \approx 0.22$) dominated by micropores ($\leq$ 2 nm). Micropores contribute to a very high specific surface area of approximately 2652 m^2/g. Three distinct pore types – tunnels, pockets, and isolated cavities – are identified in the incipient soot primary particles. The internal pore network in them is found to have a fractal dimension (D_{VC}) of approximately 2.15. Strong positive correlations between pore volume and surface area ($R^2 \approx 0.70$) are observed. The findings point to a complex and irregular external and internal structure of incipient soot nanoparticles and a complex pore network within them.

Keywords: Soot, Molecular Dynamics, Surface Fractal Dimension, Porosity, Pore Size Distribution

---

1. Introduction

Soot or black carbon is a harmful byproduct of incomplete combustion of hydrocarbon fuels [1]. It also impacts the radiative energy balance of the atmosphere and is a major forcing factor behind climate change [2, 3]. It impacts public health and welfare and is one of the leading causes of mortality worldwide [4].

The properties of the soot internal and external surfaces are important in defining how soot interacts with its surroundings. The interaction of soot with gases, pollutants, and water is influenced by its surface properties including chemical and physical properties, hydrophilicity, and charge. For

instance, the type of the soot and the environment that surrounds it, both have an effect on the adsorption behavior of the soot [5, 6, 7].

The irregular nature of soot surface and shape is often measured and represented by a suitable definition of fractal dimension. Surface fractal dimension (D_s) can be thought of as a measure of the roughness of a surface [8]. The volumetric fractal dimension (D_v) on the other hand is a measure of compactness of a soot particle. Soot particles with high surface fractal dimension (D_s) have more surface area available for adsorption and chemical reaction leading to a higher reactivity in the atmosphere [9]. The morphology of soot aggregates are often characterized by a statistical mass-fractal relationship among the primary particles, which leads to an aggregate fractal dimension (D_f) [10]. The soot aggregates with lower aggregate fractal dimension (D_f) are prone to faster aggregation and coagulation [10]. Depending on the aggregate fractal dimension (D_f), soot can affect the radiative balance of the atmosphere and cloud formation differently [11, 12]. Higher aggregate fractal dimension (D_f) in soot aggregates increases the light scattering while lower aggregate fractal dimension (D_f) increases absorption [11].

The distribution of interior cavities or pores is also crucial for understanding soot particles' interaction with the atmosphere. Cavities affect soot particle chemical reactivity, structural stability, and environmental impact. Porosity is a measure of empty space within a particle and defined as the ratio of empty space within a particle to the total volume of the particle. The empty

space within a soot particle's volume aids in adsorbing atmospheric gases like SO_2 and NO_2 affecting the aging of soot particles which influences atmospheric chemistry and pollutant transport [13, 14]. The importance of soot's porous nature and its role in atmospheric chemistry has been long recognized in the literature [15, 16, 2, 3, 17, etc.]. These earlier studies established black carbon as a significant, chemically active component of particulate matter, though the precise atomistic details of its internal structure and surface topology remained experimentally elusive. This internal structure is now understood to be a key determinant of soot's oxidative reactivity [18], while its porosity is critical for ice nucleation activity in the climate system [19] and influences the lung deposition of inhaled particles [20]. Furthermore, these same porous characteristics are leveraged in technological applications, such as optimizing the performance of carbon black in electrochemical energy storage [21]. Early studies on soot porosity has shown that soot particles with higher porosity and irregular sphericity lead to higher reactivity which can influence cloud formation and precipitation by acting as cloud condensation nuclei [6]. Moreover, when inhaled, soot particles with greater porosity are more likely to enter the lungs deeply and cause harm to the body [22].

Depending on the size, pores are classified into micropores (pores $\leq$ 2 nm) and mesopores (pores between 2 and 50 nm) [23, 24]. Micropores are smaller, but they provide very large surface area for gas adsorption and interaction with atmospheric pollutants and water vapor [25, 26]. Mesopores on the other hand, promote diffusion of larger molecules through particles and increase gas

transport into the micropores resulting in an increase in overall reactivity [26, 27, 28].

Based on the accessibility to the external surface, pores or cavities can again be classified into three groups: closed or isolated cavity that has no opening to the external surface; open or pocket cavity that has one opening to the external surface, and through or tunnel cavity which has two or more openings to the external surface [23, 24]. Figure 1 depicts a simplified diagram of a particle with different types of cavities.

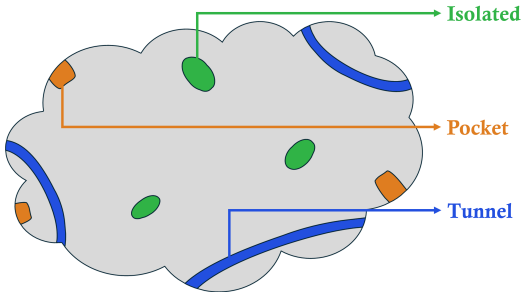

Figure 1: Schematic representation of different types of cavities inside an irregularly shaped particle.

The scale of soot particles can vary from a few nanometers [29] to a few micrometers [30] depending on fuel, environment and combustion conditions [31, 32]. Because of the small scale and dependency on the combustion conditions, it is difficult to employ experimental techniques to study different stages of soot formation and evolution of surface and internal properties [33, 34]. However, due to the recent advances in computational techniques, reactive molecular dynamics (RMD) simulations are becoming increasingly popular tools for detailed atomic-level exploration of the internal

structure of soot particles [35, 36, 37].

In this work, we investigate the surface and pore features of incipient soot primary particles using RMD simulations. This study is a continuation of our earlier works, where we established a methodology to generate and classify incipient soot particles from RMD simulations of acetylene pyrolysis. In previous studies, we characterized the overall physical, chemical, and morphological evolution of soot primary particles during inception and identified two distinct particle classes: Type 1 and Type 2 [37], where we showed that Type 2 particles possess a more developed internal structure [37, 36]. While our prior work focused on bulk properties and internal density distributions, the present study introduces a novel methodology and presents a detailed analysis of the surface topology and internal pore network of the Type 2 particles from an atomistic point of view. Specifically, the novelty of this work are: (1) The first atomistic-level classification and quantification of distinct pore archetypes (tunnels, pockets, isolated) within incipient soot particles; (2) The calculation of surface and pore fractal dimensions directly from the 3-D atomic mesh, providing a more physically representative measure of roughness and complexity than just mass-based fractal dimensions; (3) The establishment of quantitative correlations between pore volume, surface area, and particle volume, providing a pathway to incorporate these detailed features into larger-scale models. To the best of our knowledge, this level of detail in characterizing the external and internal surfaces of simulated incipient soot particles has not been previously reported. Although there have

been some experimental studies on porosity of soot or carbon black, this is, we believe, the first numerical study that quantitatively analyzes the pore structure of carbonaceous materials.

2. Methodology

The overall workflow of the present study is depicted in Fig. 2. Blocks numbered from (1) to (3) in the top box are discussed in details in our previous works [37, 36]. The tasks done in the present study are shown in blocks numbered from (4) to (7) within the bottom box.

2.1. Simulation of incipient soot particles

The Reactive Molecular Dynamics (RMD) approach (Block 1) used in this work follows the methodology presented in [38], using the specific simulation settings previously reported in detail [37, 36]. Hence, only a brief synopsis of the methodology is presented here. One thousand acetylene molecules are randomly added to a cubic domain measuring 75 Å $\times$ 75Å $\times$ 75 Å at four different temperatures: 1350, 1500, 1650, and 1800 K. This temperature range was specifically chosen to align with conditions commonly observed in experimental flow reactors [39] and laminar flames [40], and it corresponds to a critical regime in acetylene pyrolysis. As established in previous simulation studies, the 1200-1800 K range is characterized by a competition between molecular polymerization and free-radical pathways, which are crucial for the inception of soot particles [38, 41]. Temperatures below this range

primarily yield simple polymerization products like C_4H_4 and C_6H_6, while higher temperatures lead to extensive molecular cracking into H and C_2H radicals [42]. Therefore, the 1350-1800 K temperature range used in this study, thus, focuses on the key temperature window for incipient soot formation. To ensure reproducibility, every configuration was simulated at least four times using various random initial seeds for the acetylene molecules. The resulting particle populations were aggregated for statistical analysis, confirming the stability of the observed morphological features against variations in initial conditions. The reader is referred to [37, 36] for further details on the RMD simulations.

The simulations were carried out using the Large-scale Atomic/Molecular Massively Parallel Simulator (LAMMPS) software [43], utilizing the ReaxFF potential [44, 45] at a timestep of 0.25 fs. The ReaxFF methodology has been successfully applied to simulate complex pyrolysis and gasification processes for a wide range of materials, from hydrocarbons to polymers [45, 46], demonstrating its robustness in capturing high-temperature reaction chemistry. The velocity-Verlet algorithm [47] and the Nose-Hoover thermostat [48] were used in the simulations, which were run under the NVT ensemble (constant number of particles, volume, and temperature).

From each simulation, large molecular clusters were identified as incipient soot particles (Block 2). The incipient particles obtained from these simulations were validated against experimental observation in our previous

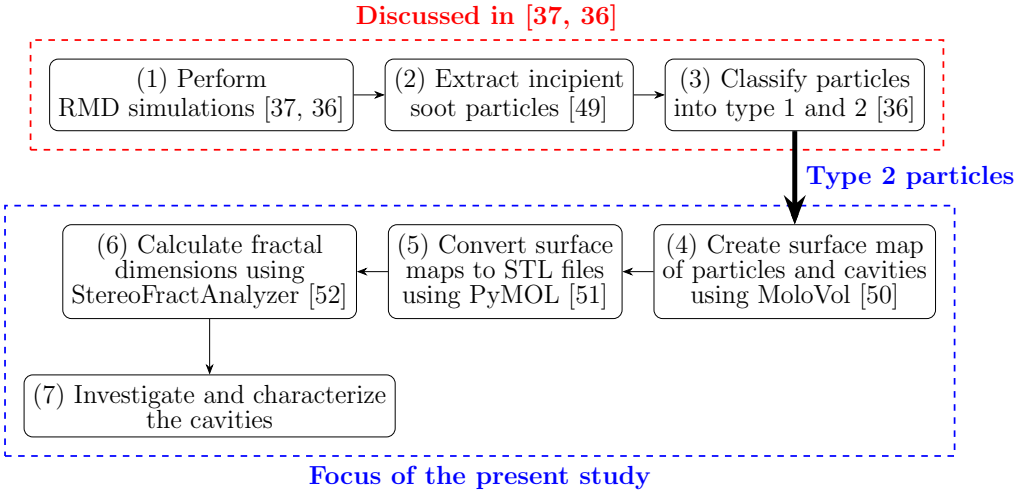

Figure 2: Overview of the workflow utilized in this work.

works [37, 36]. These particles were then classified using t-SNE [53] and k-means clustering [54], resulting in two distinct types: Type 1 and Type 2 (Block 3) [37]. Type 1 particles resemble the very early stage of soot formation where the particles are still in the process of growth by mass accumulation and surface reactions. Type 2 particles are in an advanced stage with clearly defined surface and internal structures. In this work, we only looked at the Type 2 particles because the internal structure of Type 1 particles are not yet well-developed.

While the RMD approach provides an atomistic insight, it is important to acknowledge its inherent limitations and the associated sources of uncertainty. The ReaxFF force field, while extensively validated for hydrocarbon combustion, is an empirical potential that approximates quantum mechanical interactions through a bond-order formalism [44, 55]. Its accuracy is

dependent on the parameterization, which is obtained by analyzing a finite set of quantum chemistry data [56]. Therefore, its fidelity may be lower than ab intio methods, particularly for the complex chemistry of PAH formation and the stability of certain exotic intermediates [57]. The reaction pathways observed should therefore be considered representative of the chemistry accessible within the force field's framework.

While the time step of 0.25 fs was chosen carefully to ensure energy conservation and accurately resolve high-frequency atomic vibrations, the RMD simulations are conducted on nanosecond timescales, which are orders of magnitude shorter than experimental residence times in flames or reactors. Despite these limitations, the strong agreement between our calculated morphological parameters and a wide range of experimental data reported later in this work (summarized in Table 1) along with previously reported validations in [36] provides confidence that the simulations capture the essential physical and chemical features of incipient soot particles.

2.2. Extraction of surface and pore information

From the RMD simulations, 2654 Type 2 incipient particles at four distinct temperatures were extracted. We used MoloVol [50] to extract the surface map of these particles' exterior surfaces and interior cavities (block (5) of Fig. 2). A single probe method is used to capture the surface area and surface map of the external surface while the two-probe method is used to capture both the external surface and internal cavities together. The small probe

radius is set equal to the van der Waals radius of nitrogen (1.66 Å) [58]. This choice is physically relevant for assessing molecular accessibility, as the resulting probe diameter (3.32 Å) is commensurate with the kinetic diameters of key atmospheric gas molecules such as O_2 (3.46 Å) and SO_2 (3.60 Å) [58]. This allows the probe to realistically map the surfaces and pores accessible to such species. The large probe radius is set to 5.0 Å. As discussed in the MoloVol documentation, this is a functional choice required by the two-probe method rather than a direct physical proxy. The large probe's purpose is to define the external molecular envelope of the incipient particles (which have diameters < 5 nm) without penetrating the pore network itself. By effectively 'blocking' the entrances to open pores from the outside, the large probe allows the small probe to map the internal volume of pockets and tunnels, enabling their classification [50]. The accuracy of the external surface area calculation by MoloVol was further verified with MSMS [59].

Surface maps generated using MoloVol contained details of external and internal surfaces and cavities. The surface map is then converted to a 3D surface mesh (STL format) using PyMOL [51] (block (6) of Fig. 2). This conversion is necessary to calculate the surface and volume fractal dimensions in the later steps. Two STL files are generated for each particle: one for the external surface and one for the cavities. An in-house tool called StereoFractAnalyzer [52], which calculates the fractal dimension of the surface and volume of the particles and cavities using the box-counting method [60, 61, 62, 63], is used to calculate the surface and volume fractal dimensions from the STL

files (block (7) of Fig. 2).

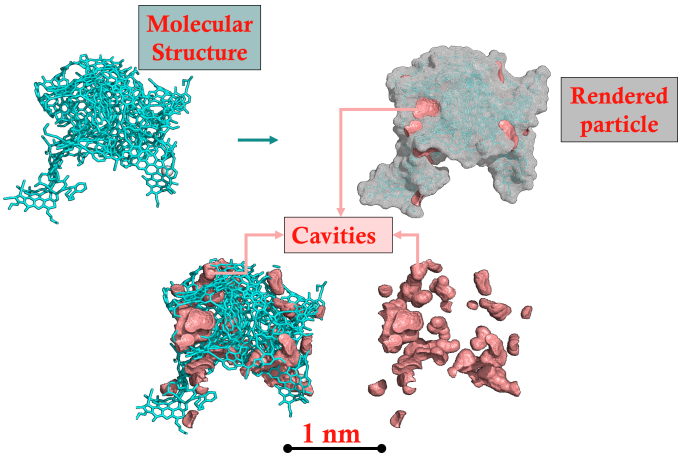

Figure 3: One example particle obtained from RMD simulations along with examples of surface renderings and identified cavities.

Additional analysis is done to explore and characterize the pores or cavities inside each particle (block (8) of Fig. 2). Fig. 3 shows the rendering of one example particle, where the external surface and cavities are shown together. The cavities are colored according to their classification: isolated cavities (green), pockets (brown), and tunnels (blue). To the best of the authors' knowledge, this is the first study to offer such detailed information regarding incipient soot particle surfaces and cavities.

In this work, the words *pore*, *void*, and *cavity* are used interchangeably to denote an empty space inside a particle.

3. Results and Discussion

We start the results section with the bulk morphological properties of the particles, followed by a detailed analysis of the distribution of cavities and their properties. Finally, we explore the correlations between surface and volume features which can potentially be useful in engineering-scale models. For the purpose of summarizing the results, we have used histograms with probability density in conjunction with box and whisker plots to show the distribution of the data. In box and whiskers plots, the box represents the interquartile range (IQR) of the data, while the whiskers represent the range of the data. The line inside the box represents the median of the data. The combination of histogram, probability density plots, and box-whiskers plots allow us to assess the variations in the distribution of each property analyzed for greater insights. The statistics are reported in the form of `mean` $\pm$ `standard error of mean (SEM)` [64] for each quantity. Standard deviation (SD) is also reported in the summary table (Table 2) for completeness.

For all the results presented in this work, the authors didn't observe any significant dependency on the temperature. Therefore, the results are presented for all the temperature cases combined. Additionally, to demonstrate the lack of temperature-dependent variation, distributions of sphericity and circularity are presented for each temperature separately. The temperature dependency is discussed in the text where necessary and reported in the Supplementary Material.

228 *3.1. Bulk morphological properties of incipient particles*

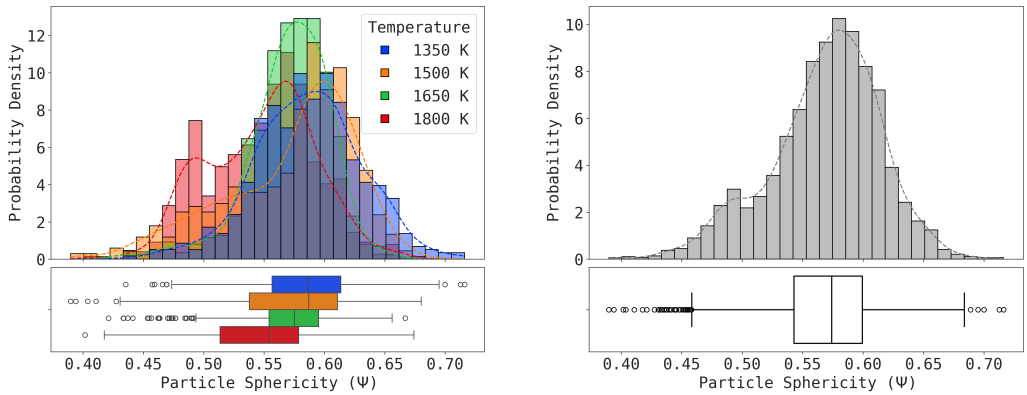

(a) At different temperatures (b) All temperatures combined

Figure 4: Distribution of sphericity (Ψ) of incipient particles.

229 Usually the soot primary particles are assumed to be perfectly spherical
230 in engineering scale models [65, 66]. However, as observed in atomic force
231 microscopy (AFM) [67] and high resolution transmission electron microscopy
232 (HRTEM) [68, 69], the incipient soot particles are not perfectly spherical.
233 The shape of the particle directly influences its reactivity particularly in
234 oxidation processes [70, 71]. How closely the shape of a particle resembles a
235 perfect sphere can be measured by sphericity (Ψ). Sphericity(Ψ) can also act
236 as an indicator of the stage of maturity of soot particle [72]. In this work,
237 Eqn. B.1 is used to calculate the sphericity of the particles.

238 The sphericity of the incipient particles is found to be 0.57 $\pm$ 0.0008. In
239 contrast, the sphericity of a perfectly spherical non-porous particle is unity.
240 The low value indicates a significantly high surface area available compared
241 to the total volume. The average sphericity of 0.57 derived here by RMD is

in reasonable agreement with the 0.63 ± 0.08 measured for larger young soot particles from premixed ethylene flames [73]. It must be noted here that presence of large number of micropores leads to a large surface area [14]. Additionally, since the surface area is calculated on an atomic level using an atomic probe, even small roughness on the surface can add to the overall surface area. Hence, even if the particle "looks" spherical, its sphericity can be significantly lower than unity. The sphericity distribution of the particles is shown in Fig. 4 using a histogram and a box-plot. The probability density of sphericity is also presented in Fig. 4 using the black-dashed line. Figure 4 provides both the distribution for each individual temperature (see Fig. 4(a)) as well as the distribution for all temperatures combined. As can be seen here, the sphericity remains almost constant at all the temperatures (Fig. 4(a)).

The histogram and the corresponding probability density function for the all-temperature-combined data in Fig. 4(b) reveal a unimodal but relatively broad distribution centered around the mean value. The interquartile range, represented by the box plot, spans from approximately 0.54 to 0.60, indicating that 50% of the particles fall within this narrow range of shapes. However, the whiskers extend from approximately 0.45 to 0.68, highlighting a significant population of particles with highly irregular, non-spherical geometries. This structural heterogeneity is a key feature of incipient soot and has direct implications for its behavior: A population of particles with diverse shapes will exhibit a wider range of reactivities and surface interaction potentials compared to a monodisperse population often assumed in engineering-scale

models. This variability underscores the importance of considering distributional properties, not just mean values, when modeling soot processes.

In practice, it is often difficult to measure the surface area of 3D microstructures. Therefore, a 2D equivalent quantity called circularity (σ) is also used in literature [74]. The definition of circularity (σ) is given in Eqn. B.2. In this study, because of asymmetry and irregularity in 3D shapes of particles, an average circularity ($\bar{\sigma}$) of each incipient particle is calculated by taking the projection of the 3D particle on to 10 evenly spaced planes in spherical coordinates as shown in Eqn. B.3. Figure 5 reports the average circularity of the incipient particles at four different temperatures including the standard deviation as error bars for each particle. Violin plots for the average circularity ($\bar{\sigma}$) of the particles at different temperatures are also presented in Fig. 5. The violin plots show that distribution is not affected by temperature (also see Fig. S.1 in the Supplementary Materials). From Fig. 5, the average circularity of the analyzed particle is found to be 0.66 ± 0.001 with an interquartile range between 0.63 and 0.68 and the maximum and minimum values of 0.48 and 0.76 which is commensurate with the variations seen in the sphericity data.

The porosity (Φ) of the particles is calculated as the ratio of the total pore volume (V_p) inside a particle to the bulk volume (V_B) of the particle (Eqn. B.4). Figure 6(a) depicts the distribution of porosity of the incipient particles using histogram with probability density and box plot. The distribution

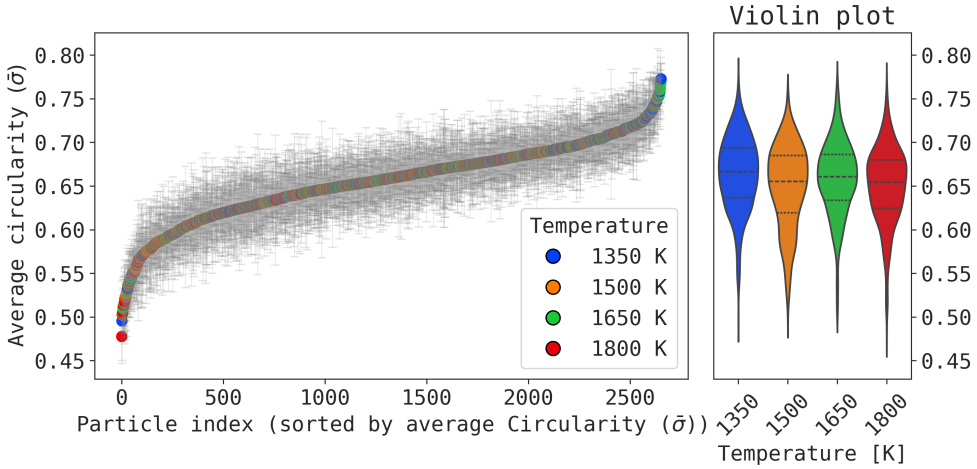

Figure 5: Average circularity ($\bar{\sigma}$) of incipient particles at four different temperatures.

is relatively narrow, with an interquartile range from approximately 0.215 to 0.225. This suggests that while the particles vary significantly in their external shape, the overall void fraction is a more conserved property across the population. The observed porosity for the incipient particles in this study is found to be 0.22 ± 0.0002, which is in good agreement with the measured soot porosity of 0.26 [75]. Temperature was found to have a very small effect on porosity (Fig. S.2 in Supplementary Materials).

Another way to look at porosity is to calculate the specific pore volume of the particles, which is a measure of available pore volume per unit mass of a particle. The specific pore volume obtained in this study is reported in Fig. 6(b). The average specific pore volume of the particles explored in this study is found to be 0.19 ± 0.0004 cm^3/g. The reported values of specific pore volume in the literature vary widely depending on the sampling proce-

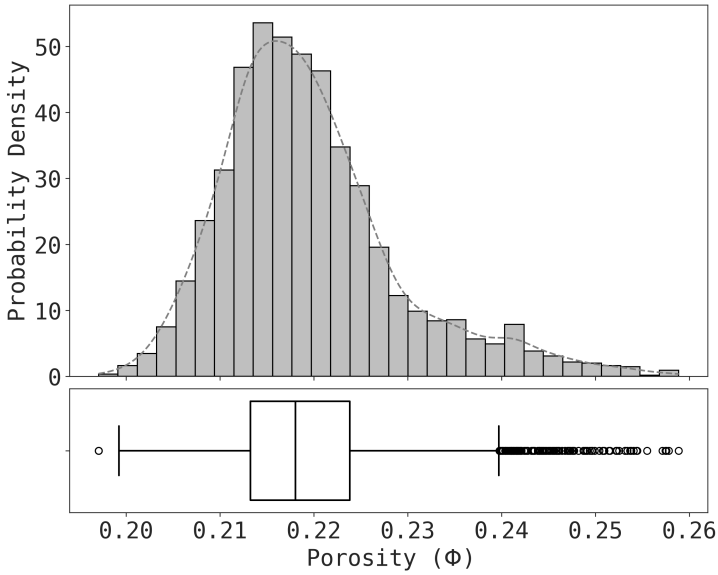

(a) Porosity, Φ

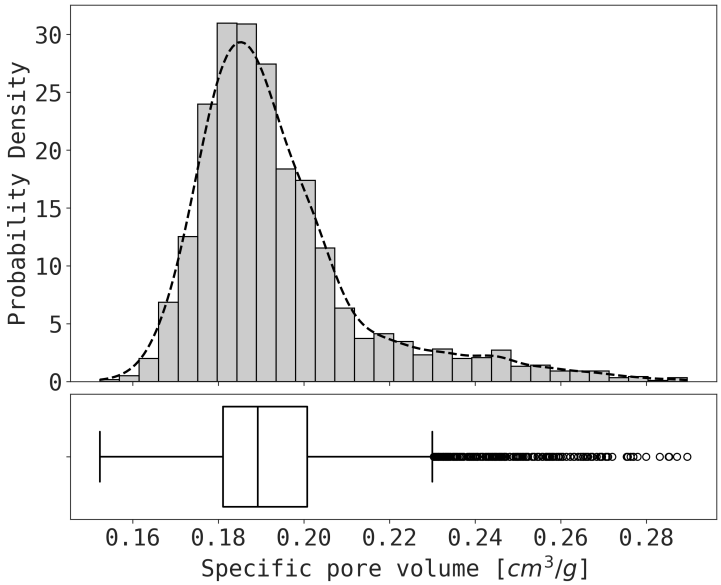

(b) Specific pore volume

Figure 6: Distribution (a) porosity, Φ and (b) specific pore volume [cm^3/g] of incipient particles.

dure, levels of maturity, and nature of pores. For example, in mature soot particles, Rockne et al. [27] reported a value of 0.004–0.08 cm^3/g for mesopores and 0.0009–0.013 cm^3/g for micropores. Whereas, Tripathi et al. [14] reported that particles with higher number of micropores can achieve specific pore volume as high as 0.7–2.3 cm^3/g. In our case, the particles are not fully mature and contain significant numbers of micropores, leading to a high value of porosity and specific pore volume. No significant temperature dependence was observed in specific pore volume (see Fig. S.3 in Supplementary Materials).

With the increase in porosity, the particles offer more accessible surface area. Specific surface area (SSA) is a measure of surface area available per unit mass. The specific surface area distribution of the incipient soot particles obtained in the current study is presented in Fig. 7. Contribution of isolated cavities is ignored in this calculation since this area is not accessible from the outside of the incipient particle. The average specific surface area of the particles is found to be 2652.36 ± 7.39 m^2/g, with an overall range (without the outliers) of 2000 – 3400 m^2/g. This value is significantly higher than the specific surface area reported in contemporary literatures. This is potentially due to several reasons. The values reported in the literature, are mostly engine-out soot particles, which are mature, larger, and have gone through some interaction with the environment. For example, Rockne et al. [27] reported the specific surface area of soot particles for mature soot particles from different combustion sources to be in the range of 1 to 85 m^2/g. Ouf

et al. [76] showed that, the specific surface area increases as the particle size decreases. Therefore, incipient particles explored in our study, which are very small and in the very early stage of formation, are expected to have higher specific surface area. Also, the presence of numerous micropores in the particles, which is the case in the particles in this work, can lead to higher surface area, which in turn lead to higher specific surface area [14]. Additionally, high values of SSA has been reported in high surface area carbon materials such as activated carbons derived from biomass (SSAs of up to 3386 m^2/g [77]), metal-organic-framework (MOF)-derived carbons (up to 2872 m^2/g [78]), and hypercrosslinked polymer-derived carbons (up to 4300 m^2/g [79]). These examples illustrate that materials with high porosity can achieve exceptionally high SSAs, supporting the elevated SSA observed in our incipient soot particles.

The theoretical specific surface area ($SSA_{\text{Theoretical}}$) for the external surface of a spherical particle can be calculated using the volume-equivalent diameter (d_V) of the particle and its bulk density (ρ_b) as shown in Eqn. B.5. The average theoretical specific surface area ($\overline{SSA}_{\text{Theoretical}}$) of the particles is found to be 1493.77 m^2/g and is shown in Fig. 7 as a red dashed vertical line. Equation B.5 describes the theoretical minimum external specific surface area of a perfect smooth sphere with no surface cavities. Notably, the measured median specific surface areas for our incipient soot particles exceed this theoretical minimum by almost a factor of two. This highlights the significant contribution of porosity and complex surface morphology to the total

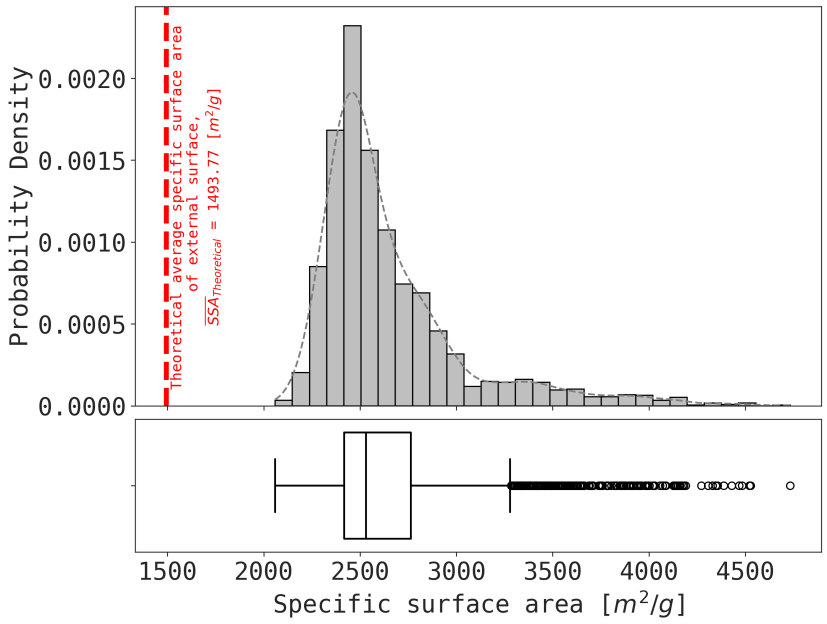

Figure 7: Distribution of specific surface area [m^2/g] of incipient particles.

accessible surface area. Additionally, Eqn. B.5 shows that SSA is inversely proportional to the volume-equivalent diameter (d_V), meaning that smaller particles inherently possess higher external surface area per unit mass. Since our incipient particles are in the very early stage of formation and small (diameters < 5 nm), their baseline external surface area (A_{Ext}) is already high. However, the fact that our measured SSAs surpass the theoretical value clearly illustrates that besides direct surface effects, porosity further elevates the overall accessible surface area. No specific trend is observed with temperature (Supplementary Materials, Fig. S.4) for specific surface area.

To further elucidate the influence of internal porosity on the overall accessible

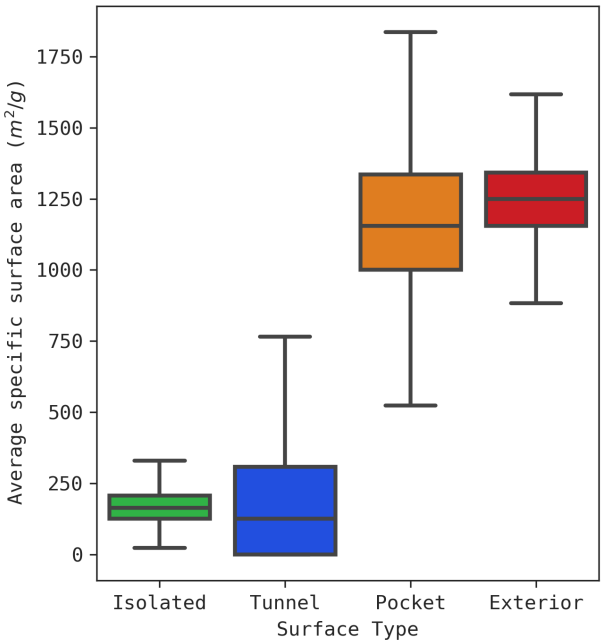

Figure 8: Contribution of different cavities to specific surface area [m^2/g] of incipient particles.

surface area, we decompose the total SSA into contributions from distinct cavity types as well as the exterior surface area (ESA), which represents the surface area calculated without any cavity contributions (note the difference between *external* and *exterior* surface area: exterior surface does not include any contributions from cavities, whereas external surface includes the exposed surface of tunnels and pockets). The SSA values presented in Fig. 7 include contributions from tunnel and pocket cavities. Figure 8 separately illustrates the SSA for each cavity type (tunnel, pocket, isolated) alongside the ESA. The comparison between the ESA and the cavity contributions clearly demonstrates that the enhanced SSA observed in our incipient soot particles is largely due to the presence of pockets. The average specific surface areas are: 172.36 ± 1.34 m^2/g for isolated cavities, 212.12 ± 5.43 m^2/g for tunnel cavities, 1190.94 ± 5.71 m^2/g for pocket cavities, and 1249.29 ± 2.84 m^2/g for the exterior surface. This decomposition not only emphasizes the significant role played by tunnel and pocket cavities in increasing the accessible surface area, but also provides insight into the interplay between particle size and internal morphology. No specific trend is observed with temperature (Supplementary Materials, Fig. S.5).

3.2. Bulk morphological properties of pores

As discussed earlier, depending on the access to the surface of incipient particles, the pores are classified into three groups: tunnels, pockets, and isolated cavities. These classifications provide insight into the way different cavities

interact with the environment. Following Eqn. B.1, the sphericity of each cavity can also be calculated. To compare the statistics of all the particles together, we calculated the average pore sphericity ($\bar{\psi}$) of different classes of cavities for each particle using Eqn. B.6.

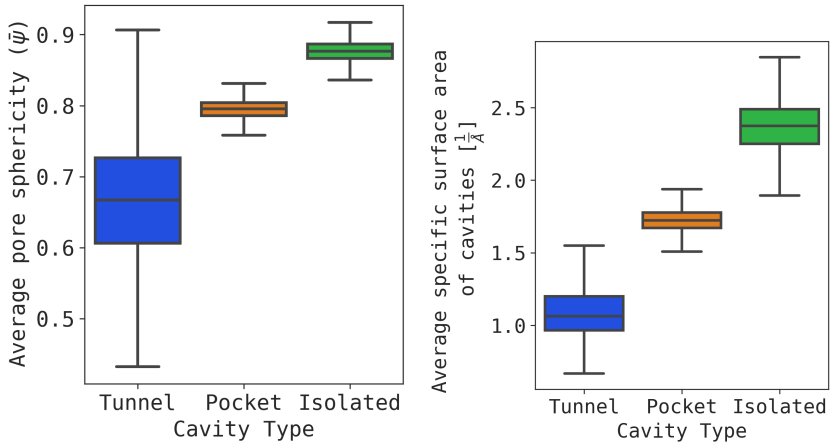

(a) Average pore sphericity, $\bar{\psi}$ (b) Average specific surface area of cavities (1/Å)

Figure 9: (a) Average pore sphericity, $\bar{\psi}$ and (b) average specific surface area of cavities [1/Å] in incipient particles.

Figure 9(a) shows clear distinction among the average pore sphericity of different cavities. The average pore sphericity of tunnels, pockets, and isolated cavities are found to be 0.67 ± 0.002, 0.80 ± 0.0002, and 0.88 ± 0.00003, respectively. This indicates that, the isolated cavities are more spherical than the pockets and tunnels, which are more elongated due to their openings to the external surface. The interquartile range and whiskers for pockets and isolated cavities are much smaller than that of tunnels indicating a much larger variation in the shape of tunnels than pockets and isolated cavities.

Since cavities do not have any mass, the surface area of different cavities are quantified using a volume-based specific surface area which is defined as the amount of cavity surface area per unit volume of the cavity. Thus, the unit for this volume-based surface area is Å^{-1}. Figure 9(b) depicts the average volume-based specific surface area of different cavities. Unlike Fig.8, where SSA is computed by aggregating the contributions of all cavities across all particles, here the volume-based SSA is first averaged over all cavities within each individual particle and then further averaged across all particles. This procedure preserves information regarding the typical size or footprint of each cavity type within incipient soot particles. As observed with pore sphericity, different cavities shows clear distinction. The average specific surface area of tunnels, pockets, and isolated cavities are found to be 1.1 ± 0.005, 1.72 ± 0.002, and 2.38 ± 0.03 Å^{-1}, respectively. Since isolated cavities are more spherical than the other two types, they also have the highest specific surface area than pockets and tunnels. Both average pore sphericity ($\bar{\psi}$) and specific surface area of the cavities are found to be independent of temperature (See Supplementary Materials Fig. S.6).

3.3. Fractal characteristics of incipient particles and cavities

The fractal dimension is an important metric for characterizing the complexity and self-similarity of a structure. In the context of soot particles, usually the fractal dimension is reported for the soot aggregates, which are formed by the agglomeration of primary particles. This fractal dimension, also known as

aggregate fractal dimension (D_f) is calculated using a statistical mass-fractal relationships [11, 80]. In this work, we are not investigating this definition of fractal dimension of an aggregate, rather we are focusing on the fractal dimensions of an individual primary particle. While the fractal dimension of soot aggregates has been extensively studied, the fractal dimensions of primary particles is less commonly reported. Understanding the fractal nature of individual primary particle morphology provides valuable insights into the early stages of soot formation, which can inform more accurate models of soot reactivity and growth. In this work, we analyzed surface and volume fractal dimension (D_S and D_V) of incipient primary particles.

The surface fractal dimension (D_S) of the incipient particle describes how the particle's surface scales as its size increases. A smooth surface would have a surface fractal dimension value of 2. A higher surface fractal dimension indicates a rougher, more irregular surface, which increases the available surface area for chemical interactions. The surface fractal dimension of the particles is found to be 2.22 ± 0.001, which is in excellent agreement with the $D_S = 2.25 \pm 0.09$ measured for carbon black [81, 82] and indicating a highly irregular and rough surface of the incipient particles. The distribution of the surface fractal dimension of the incipient particles is shown in Fig. 10(a). The narrow unimodal nature of this distribution suggests that a surface roughness corresponding to $D_S \approx 2.22$ is an almost-conserved and fundamental feature of these nascent particles, largely independent of their individual size or overall shape. The surface fractal dimension of the particles is found to be

independent of temperature (Supplementary Materials, Fig. S.7).

The volume fractal dimension (D_V) can be thought of as the ability to self-similarly fill the space by a solid [83]. With a higher value of volume fractal dimension (D_V), the particle is more compact and less porous. The distribution of volume fractal dimension of the incipient particles is shown in Fig. 10(b). Similar to the surface fractal dimension, the narrowness of this distribution suggests that the particle's compactness is a highly conserved structural feature, with most particles clustering tightly around the mean value of $D_V \approx 2.53$. The volume fractal dimension of the particles is found to be 2.53 ± 0.0006 in the present study. This indicates that the incipient particles are highly porous and have a complex internal structure. The volume fractal dimension of the particles is found to be independent of temperature (Supplementary Materials, Fig. S.8). It should be noted here that previously Mukut et al. [37, 36] reported an atomic fractal dimension of these incipient primary particles, which was calculated as a mass-based fractal dimension (i.e., ability of a particle to self-similarly contribute to particle mass) for primary particle.

The fractal characteristics of the cavities provide insights into the complexity of the internal pore networks. These networks influence the ability of the particles to adsorb gases and engage in chemical reactions. A lower surface fractal dimension for the cavities (D_{SC}) suggests a smoother internal surface compared to the external particle surface, which may affect the overall reac-

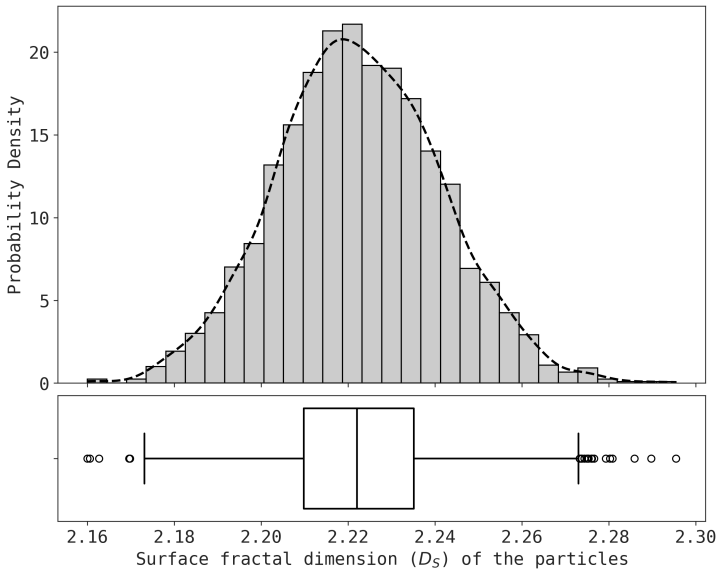

(a) Surface fractal dimension (D_S) of the particles

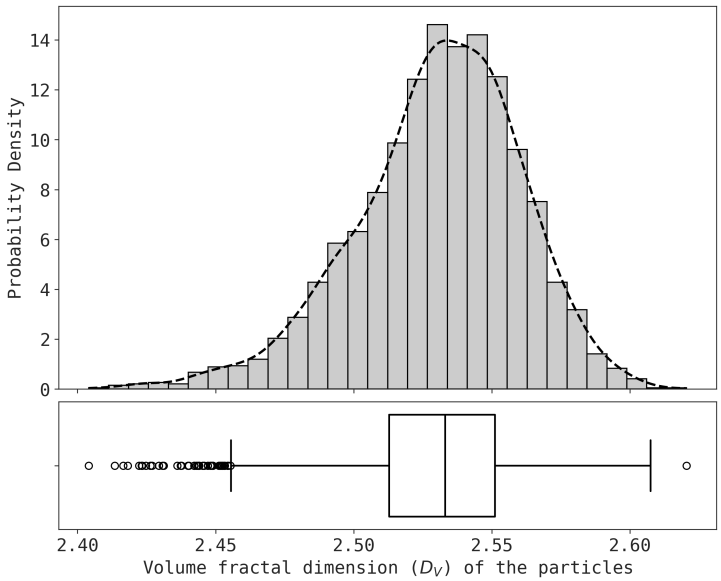

(b) Volume fractal dimension (D_V) of the particles

Figure 10: Distribution of (a) surface fractal dimension (D_S), and (b) volume fractal dimension (D_V) of incipient particles.

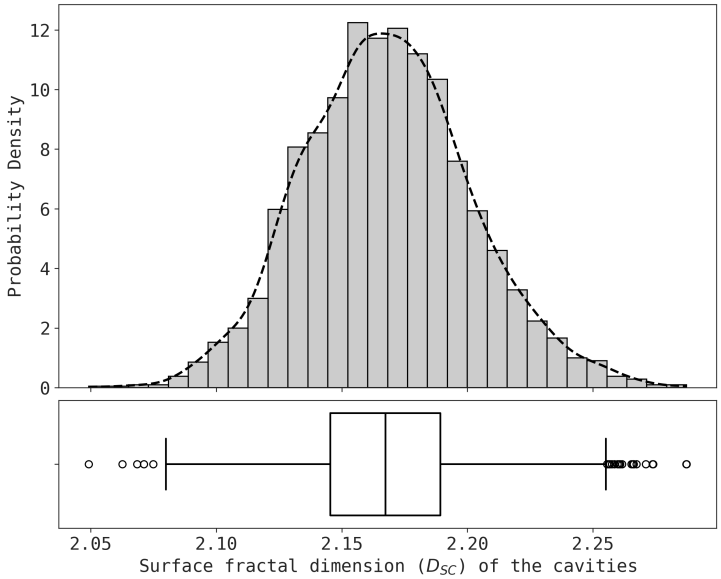

(a) Surface fractal dimension (D_{SC}) of the cavities

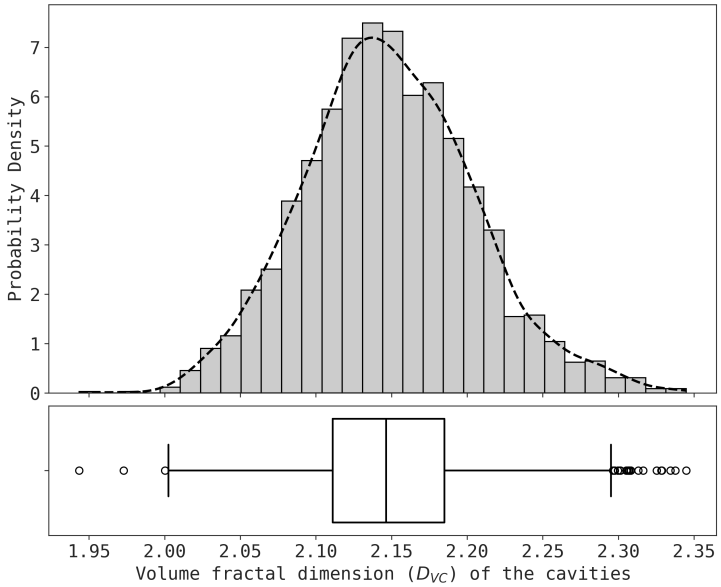

(b) Volume fractal dimension (D_{VC}) of the cavities

Figure 11: Distribution of (a) surface fractal dimension (D_{SC}), and (b) volume fractal dimension (D_{VC}) of the cavities within incipient particles.

tivity and interaction with the environment. The surface fractal dimension (D_{SC}) and volume fractal dimension (D_{VC}) of different cavities are calculated using the same method as for the particles. As shown in Fig. 11(a), the surface fractal dimension of the cavities is found to be 2.17 $\pm$ 0.006. In contrast to the particle surface, the cavity surface is slightly more regular and less rough. This is also reflected in the higher average cavity sphericity ($\bar{\psi}$) value shown in Fig. 9(a).

The volume fractal dimension of cavities (D_{VC}) is commonly referred to as the pore fractal dimension. This is a measure of complexity of internal pore network inside soot particles which quantify how the empty space within a primary particle is self-similarly distributed within the particle [84]. It has been reported in the literature that the pores of soot and carbon blacks form a fractal-like network with pore fractal dimension of between 2–2.5 as measured using small angle X-ray scattering (SAXS) [85], Ar, CO_2, and N_2 adsorption studies [86, 21], and numerical studies of soot oxidation [87]. The volume fractal dimension (D_{VC}) of the cavities in this work is found to be 2.15 $\pm$ 0.001, which is in excellent agreement with the reported values. The distribution of volume fractal dimension of cavities (D_{VC}) observed in the present study is shown in Fig. 11(b). Both the surface and volume fractal dimensions of the cavities are found to be independent of temperature (Supplementary Materials, Figs. S.9 and S.10).

These fractal dimensions have direct implications for the real-world behavior

of soot. The high surface fractal dimension ($D_s \approx 2.22$) indicates a highly convoluted and rough external surface, which significantly increases the number of active sites and the total surface area available for heterogeneous reactions. This enhanced surface area promotes higher rates of oxidation by species like O_2 and OH and increases the particle's capacity for adsorbing atmospheric pollutants such as SO_2 and NO_x [5, 6]. The complex internal network, characterized by the pore fractal dimension ($D_{VC} \approx 2.15$), provides additional pathways for gas transport into the particle interior, further influencing its overall reactivity [87]. Additionally, the pore fractal dimension and surface area derived here may enable models for soot oxidation to move beyond simple surface reactions and account for the realistic porosity of incipient nanoparticles, thereby deriving more robust oxidation rates [71]. Although this study focuses only on primary particles, an accurate characterization of fractal nature of primary particles is necessary for better characterization and understanding of the fractal nature of the soot aggregate. The morphology of these aggregates, described by an aggregate fractal dimension (D_f), governs their optical and aerodynamic properties. More open and lacy aggregates (lower D_f) are known to scatter more light than compact structures (higher D_f), which in turn affects their radiative forcing in the atmosphere [11, 80, 12, 3].

3.4. Summary of experimental validation

As has been discussed in earlier sections, morphological features of the simulated incipient particles were compared with experimental data where available. A summary of these comparisons is provided in Table 1, which shows a strong correspondence between our computationally derived values and experimentally measured properties for various carbonaceous materials. The close agreement across these distinct morphological parameters provides confidence in the physical realism of the incipient soot structures generated by the RMD simulations.

Table 1: Comparison of simulated morphological properties with experimental data.

Property	**RMD simulations (this work)**	**Experimental value**	**Reference(s)**
Particle porosity (Φ)	0.22 ± 0.0002	0.26	Song et al. [75]
Particle sphericity (Ψ)	0.57 ± 0.0008	0.63 ± 0.08	Schenk et al. [73]
Particle surface fractal dimension (D_s)	2.22 ± 0.001	2.25 ± 0.09	Avnir et al. [82], Kandas et al. [85]
Pore fractal dimension (D_{VC})	2.15 ± 0.001	2.0 - 2.5	Ehrburger-Dolle et al. [86], Kelesidis et al. [21]

3.5. Pore size distribution inside incipient particles

Understanding the distribution of pore sizes within soot particles can provide insights into their formation mechanisms and behavior in different combustion environments. The cavity size in this work is represented by the volume-equivalent pore diameter (d_p), which represents the diameter of a sphere with an equivalent volume to the cavity. The distribution of individual cavity sizes (d_p) in the entire population is shown in Fig. 12. The distribution is log-normal, which indicates that although there are a few

larger cavities, most cavities are small: which is typical for porous structures. Additionally, it can be seen that all cavities identified in this study are micropores ($\leq$2 nm), with the majority measuring less than 1 nm. This is expected since all the incipient particles investigated here are in the very early stage of formation and have a diameter smaller than 5 nm. This essentially makes micropores the primary focus of this analysis. As has been discussed earlier, such large presence of micropores increases the surface area leading to high specific surface area, high porosity, and low sphericity values observed in the incipient particles, which is typical of soot particles in the early stages of formation [14].

This distribution of cavity size (i.e., d_p) can also be analyzed by calculating the average values for cavity sizes ($\overline{d_p}$) inside each particle. The tunnel cavities have the largest average size (8.92 $\pm$ 0.05 Å), followed by pockets (4.85 $\pm$ 0.006 Å) and isolated (3.08 $\pm$ 0.005 Å) cavities. The size distribution of average cavity sizes ($\overline{d_p}$) (shown in Supplementary Materials, Fig. S.11) is a Gaussian distribution, as is expected, since averaging tends to smooth out variability.

To get a more complete understanding of the pore network of the particles, the average fraction of void volume occupied by cavities of different sizes within incipient particles is calculated and shown in Fig. 13. Figure 13 shows that the pocket cavities occupy the largest fraction of void volume, followed by isolated cavities and tunnels. Although tunnels are larger on average

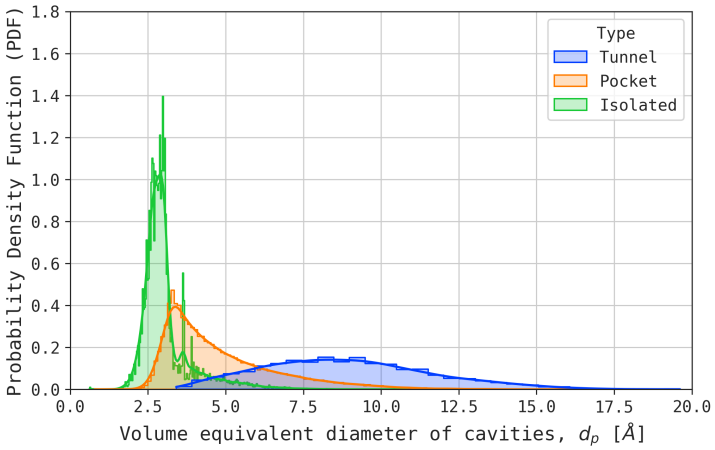

Figure 12: Cavity size (d_p) distribution of all cavities across all the particles.

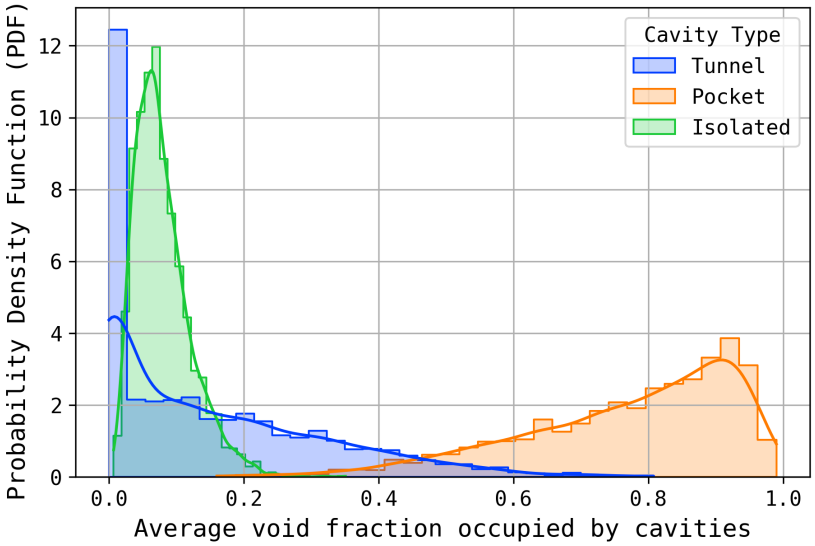

Figure 13: Distribution of average fraction of void volume occupied by cavities of different sizes within incipient particles.

(Supplementary Materials, Fig. S.11), their lower abundance in the incipient particles results in them occupying a smaller fraction of the overall void volume. In contrast, the higher abundance of pocket cavities allows them to occupy a larger portion of the void space, despite their smaller size. The pockets and tunnels present in the bulk particles are critical for the oxidation of soot and carbon black at low temperatures (e.g. 550 °C) [21]. At these conditions, O_2 can diffuse through these pockets and tunnels and internally oxidize soot and carbon black nanoparticles, resulting in hollow spheres [21, 87].

In the porous material literature, the pore size distribution (PSD) is often reported in terms of cumulative void volume (per unit mass) as a function of pore size [88, 89]. Cumulative void volume ($V_C(d_p)$) refers to the total volume of empty spaces accumulated within a particle up to specific cavity sizes (d_p) and is calculated using Eqn. B.7.

Each particle will produce a different pore size distribution. To present the data in a compact form, we have calculated the average PSD from all the particles by dividing the diameter range into discrete size bins and calculating the cumulative volume of cavities in each bin for all the particles. The average PSD of different cavities is shown in Fig. 14. The shaded region in Fig. 14 represents the standard error of the mean (SEM). The average PSD of isolated cavities is shifted towards smaller pore sizes, while that of pocket and tunnel cavities is shifted towards larger pore sizes. For the sake

of completeness, the un-averaged PSD of the entire population of cavities is also provided in Fig. S.12.

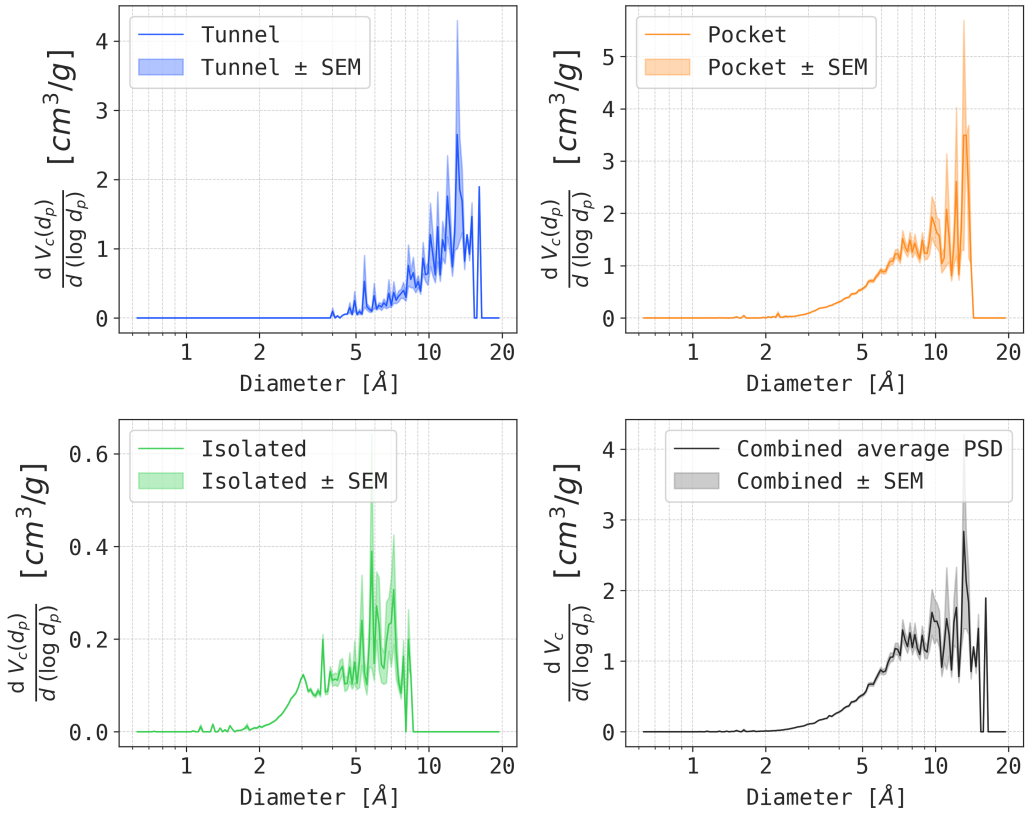

Figure 14: Average pore size distribution (PSD) of different cavities within incipient soot primary particles.

3.6. Correlations for pore area and pore volume

Engineering scale soot models usually carry information about the volume of soot particles [66, 90], which does not, on its own, include any information on the pores. If some correlations can be drawn between the volume and surface area of pores and the particle volume, some critical information on

the pore network within a particle can be extracted, which can improve the modeling of chemical reactivities of soot particles. A good positive correlation ($R^2 \approx 0.70$) between total pore volume (V_p) and total pore surface area (A_p) was found (see Supplementary Materials, Fig. S.13). No significant temperature dependence is observed in this correlation.

Similarly, the particle's material volume (V) and total pore volume (V_p) (Supplementary Material, Fig. S.14), shows a positive and generally linear correlation. However, the correlation shows a weaker correlation coefficient ($R^2 \approx 0.60$) than the correlation between pore volume (V_p) and pore surface area (A_p). This suggests that while particle size is a significant factor in determining pore volume (V_p), other factors may also play a role. A slight change in correlation is also observed with process temperature, as shown in the Supplementary Materials (Fig. S.14).

Finally, individual pore volume (V_{pi}) and pore surface area (A_{pi}) shows a strong positive and linear correlation, with high correlation coefficients ($R^2 \approx 0.98$, depicted in Supplementary Materials, Fig. S.15), indicating that larger cavities have proportionally greater surface areas. This correlation is independent of cavity types, highlighting that cavity size is a dominant factor in determining pore surface area, regardless of the type of cavity. The equations for the linear correlations (for all temperature combined) are given in Correlation Set 1. An exponential and a quadratic fit were also explored, but no significant improvement of correlation coefficient were observed. These

correlations provide valuable insights into how particle morphology and pore structure evolve, with implications for modeling the surface area and reactivity of soot particles in different environmental and combustion scenarios.

Correlation Set 1: Temperature-independent equations of curves fitted to the pore volume, pore surface area, and particle volume (data shown in Supplementary Materials, Figs. S.13, S.14,and S.15). Here, V is the particle's material volume [Å^3], V_p is the total pore volume within an incipient particle [Å^3], A_p is the total pore surface area [Å^2], V_{pi} is the volume of an individual pore [$\mathring{A}^3$], and A_{pi} is the surface area of an individual pore [$\mathring{A}^2$].

$$A_p = 1.39V_p - 335.53, \qquad R^2 = 0.70, \tag{1}$$

$$V_p = 0.16V + 277.52, \qquad R^2 = 0.57, \tag{2}$$

$$A_{pi} = 0.89V_{pi} + 30.20, \qquad R^2 = 0.98 \tag{3}$$

3.7. Summary statistics

The summary statistics is presented in Table 2, which shows the mean, standard error of the mean (SEM) and standard deviation (SD) of the surface and pore features of incipient particles. The table provides a comprehensive overview of the key properties of the particles, including sphericity, porosity, specific pore volume, specific surface area, average pore sphericity, average specific surface area of different cavities, surface fractal dimension, volume fractal dimension, and average volume equivalent diameter of different cav-

Table 2: Mean, Standard Error of the Mean (SEM), and Standard Deviation (SD) of the surface and pore features of incipient particles.

Property	**Unit**	**Statistics**				
		Mean	±	SEM	SD
Particle sphericity, Ψ	–	0.57	±	0.0009	0.046
Particle average circularity, $\bar{\sigma}$	–	0.655	±	0.001	0.044
Porosity, Φ	–	0.22	±	0.0002	0.01
Specific pore volume	cm^3/g	0.194	±	0.0004	0.02
Specific surface area of particle	m^2/g	2652.36	±	7.388	380.62
Average pore sphericity for tunnels cavities, $\bar{\psi}_{Tunnel}$	–	0.665	±	0.002	0.088
Average pore sphericity for pockets cavities, ψ_{Pocket}	–	0.795	±	0.0002	0.014
Average pore sphericity for isolated cavities $\psi_{Isolated}$	–	0.877	±	0.0003	0.016
Average specific surface area of tunnel cavities (mass-based)	m^2/g	212.12	±	5.43	279.63
Average specific surface area of pocket cavities (mass-based)		1190.94	±	5.71	294.17
Average specific surface area of isolated cavities (mass-based)		172.36	±	1.34	69.07
Average specific surface area of tunnel cavities (volume-based)	$\frac{1}{Å}$	1.096	±	0.005	0.196
Average specific surface area of pocket cavities (volume-based)		1.723	±	0.002	0.084
Average specific surface area of isolated cavities (volume-based)		2.374	±	0.004	0.193
Surface fractal dimension of particle, D_S	–	2.223	±	0.0003	0.019
Volume fractal dimension of particle, D_V	–	2.531	±	0.001	0.03
Surface fractal dimension of cavity, D_{SC}	–	2.168	±	0.001	0.033
Volume (Pore) fractal dimension of cavity, D_{VC}	–	2.149	±	0.001	0.056
Average volume equivalent diameter of tunnels cavities	Å	8.918	±	0.055	2.359
Average volume equivalent diameter of pockets cavities		4.854	±	0.006	0.329
Average volume equivalent diameter of isolated cavities		3.078	±	0.005	0.262

ities. These statistics can be used to develop more accurate models of soot formation and reactivity, with implications for environmental and combustion studies.

4. Conclusion

We present a novel and transferable computational framework to extract detailed information on the external surface and internal pores from the atomic structures of nanostructured carbon materials. The framework and tools developed and presented in this work can be adopted to analyze surface and pore features of any atomic structures as long as an atomistic description of the structure is available. In this work, such atomistic descriptions of

soot primary particles were obtained using RMD simulations. By integrating RMD simulations with atomistic-scale surface and pore analysis, this work offers a novel approach for characterizing a wide range of materials, from combustion-generated soot and carbon black to engineered materials like biochars and porous carbons used in catalysis, gas adsorption [77, 78], energy generation [91] and storage [92]. The detailed quantification of fractal dimensions, porosity, and specific surface area provides valuable descriptors for modeling gas-solid interactions, pollutant transport, and interfacial phenomena in complex carbonaceous systems.

In this study, over 2000 incipient soot particles formed during RMD simulations of acetylene pyrolysis were analyzed. The analysis revealed a highly porous ($\Phi \approx 0.22$) and irregular structure of soot primary particles, characterized by a surface fractal dimension of $D_S \approx 2.22$ and a pore fractal dimension of $D_{VC} \approx 2.15$. The internal pore network is dominated by micropores (≤ 2 nm), with pocket-type cavities being the most significant contributors to the total void volume. The large presence of micropores potentially increased the available surface area, leading to a high value of specific surface area of approximately 2652.36 m^2/g and a low value of sphericity (around 0.57). In all analysis presented here, no significant impact of process temperature was found among the temperatures studied. This minimal temperature dependence observed suggests a stable early-stage structural configuration across different combustion conditions.

These findings have significant implications for understanding soot behavior. The high specific surface area driven by high microporosity, suggests that incipient soot may possess a much higher potential for gas adsorption and heterogeneous chemical reactions than is typically assumed in models that treat primary particles as non-porous spheres. The prevalence of accessible pores (pockets and tunnels) provides pathways for oxidants like O_2 to penetrate the particle interior, facilitating internal oxidation and influencing the particle's ultimate fate in combustion and atmospheric environments [21].

The strong positive correlations observed between pore volume, pore surface area, and particle material volume offer a practical means to incorporate these detailed morphological features into engineering-scale soot models, which traditionally track only bulk properties like mass or volume. Implementing these proposed correlations can improve predictive accuracy for soot reactivity and aging.

Future research should extend this framework to investigate the evolution of these pore and surface features during soot maturation and oxidation. By simulating the interaction of these detailed particle structures with oxidants like O_2 and OH, it will be possible to directly link specific morphological features, such as the prevalence of pocket cavities, to overall particle reactivity. Additionally, application of this methodology to soot formed from different fuels (e.g., aromatics, biofuels) will shed light on how fuel chemistry dictates the nascent particle morphology. This research contributes to the

growing body of research that aims to develop a source-structure-property relationship for carbonaceous nanoparticles which can be integrated into next-generation of detailed and predictive soot models.

5. Acknowledgments

K.M.M. and S.P.R. wishes to thank Mr. Anindya Ganguly (University of Melbourne) for providing the RMD trajectory files from which the particles were extracted for analysis. The research benefited from computational resources provided through the NCMAS, supported by the Australian Government, The University of Melbourne's Research Computing Services and the Petascale Campus Initiative. K.M.M. and S.P.R. acknowledge funding support from the National Science Foundation as some of this material is based upon work supported by the National Science Foundation under Grant No. 2144290.

References

[1] H. A. Michelsen, M. B. Colket, P.-E. Bengtsson, A. D'Anna, P. Desgroux, B. S. Haynes, J. H. Miller, G. J. Nathan, H. Pitsch, H. Wang, A Review of Terminology Used to Describe Soot Formation and Evolution under Combustion and Pyrolytic Conditions, ACS Nano 14 (10) (2020) 12470–12490. doi:10.1021/acsnano.0c06226.

[2] J. Hansen, L. Nazarenko, Soot climate forcing via snow and ice albedos,

676 Proc. Natl. Acad. Sci. U.S.A. 101 (2) (2004) 423–428. doi:10.1073/
677 pnas.2237157100.

678 [3] T. C. Bond, S. J. Doherty, D. W. Fahey, P. M. Forster, T. Berntsen,
679 B. J. DeAngelo, M. G. Flanner, S. Ghan, B. Kärcher, D. Koch, S. Kinne,
680 Y. Kondo, P. K. Quinn, M. C. Sarofim, M. G. Schultz, M. Schulz,
681 C. Venkataraman, H. Zhang, S. Zhang, N. Bellouin, S. K. Guttikunda,
682 P. K. Hopke, M. Z. Jacobson, J. W. Kaiser, Z. Klimont, U. Lohmann,
683 J. P. Schwarz, D. Shindell, T. Storelvmo, S. G. Warren, C. S. Zender,
684 Bounding the role of black carbon in the climate system: A scientific
685 assessment, Journal of Geophysical Research: Atmospheres 118 (11)
686 (2013) 5380–5552. doi:10.1002/jgrd.50171.

687 [4] B. Brunekreef, M. Strak, J. Chen, Z. J. Andersen, R. Atkinson,
688 M. Bauwelinck, T. Bellander, M.-C. Boutron, J. Brandt, I. Carey,
689 G. Cesaroni, F. Forastiere, D. Fecht, J. Gulliver, O. Hertel, B. Hoff-
690 mann, K. de Hoogh, D. Houthuijs, U. Hvidtfeldt, N. Janssen, J. Jor-
691 gensen, K. Katsouyanni, M. Ketzel, J. Klompmaker, N. H. Krog,
692 S. Liu, P. Ljungman, A. Mehta, G. Nagel, B. Oftedal, G. Pershagen,
693 A. Peters, O. Raaschou-Nielsen, M. Renzi, S. Rodopoulou, E. Samoli,
694 P. Schwarze, T. Sigsgaard, M. Stafoggia, D. Vienneau, G. Weinmayr,
695 K. Wolf, G. Hoek, Mortality and Morbidity Effects of Long-Term Expo-
696 sure to Low-Level PM2.5, BC, NO2, and O3: An Analysis of European
697 Cohorts in the ELAPSE Project (Research Report (Health Effects In-

stitute), 208) (2021) 1–127, PMID: 36106702.
URL https://pubmed.ncbi.nlm.nih.gov/36106702

[5] A. R. Chughtai, M. M. O. Atteya, J. Kim, B. K. Konowalchuk, D. M. Smith, Adsorption and adsorbate interaction at soot particle surfaces, Carbon 36 (11) (1998) 1573–1589. doi:10.1016/S0008-6223(98)00116-X.

[6] O. Popovicheva, N. M. Persiantseva, N. K. Shonija, P. DeMott, K. Koehler, M. Petters, S. Kreidenweis, V. Tishkova, B. Demirdjian, J. Suzanne, Water interaction with hydrophobic and hydrophilic soot particles, Phys. Chem. Chem. Phys. 10 (17) (2008) 2332–2344. doi:10.1039/B718944N.

[7] M. E. Monge, B. D'Anna, L. Mazri, A. Giroir-Fendler, M. Ammann, D. J. Donaldson, C. George, Light changes the atmospheric reactivity of soot, Proc. Natl. Acad. Sci. U.S.A. 107 (15) (2010) 6605–6609. doi:10.1073/pnas.0908341107.

[8] P. Pfeifer, Fractal dimension as working tool for surface-roughness problems, Applications of Surface Science 18 (1) (1984) 146–164. doi:10.1016/0378-5963(84)90042-4.

[9] Z. Li, C. Song, J. Song, G. Lv, S. Dong, Z. Zhao, Evolution of the nanostructure, fractal dimension and size of in-cylinder soot during

diesel combustion process, Combust. Flame 158 (8) (2011) 1624–1630. doi:10.1016/j.combustflame.2010.12.006.

[10] G. Skillas, S. Künzel, H. Burtscher, U. Baltensperger, K. Siegmann, High fractal-like dimension of diesel soot agglomerates, J. Aerosol Sci. 29 (4) (1998) 411–419. doi:10.1016/S0021-8502(97)00448-5.

[11] L. Liu, M. I. Mishchenko, W. Patrick Arnott, A study of radiative properties of fractal soot aggregates using the superposition T-matrix method, J. Quant. Spectrosc. Radiat. Transfer 109 (15) (2008) 2656–2663. doi:10.1016/j.jqsrt.2008.05.001.

[12] Y. Wang, F. Liu, C. He, L. Bi, T. Cheng, Z. Wang, H. Zhang, X. Zhang, Z. Shi, W. Li, Fractal Dimensions and Mixing Structures of Soot Particles during Atmospheric Processing, Environ. Sci. Technol. Lett. 4 (11) (2017) 487–493. doi:10.1021/acs.estlett.7b00418.

[13] B. Hu, U. Koylu, Size and Morphology of Soot Particulates Sampled from a Turbulent Nonpremixed Acetylene Flame, Aerosol Sci. Technol. (Oct. 2004).
URL https://www.tandfonline.com/doi/abs/10.1080/027868290519111

[14] P. K. Tripathi, M. Liu, Y. Zhao, X. Ma, L. Gan, O. Noonan, C. Yu, Enlargement of uniform micropores in hierarchically ordered mi-

cro–mesoporous carbon for high level decontamination of bisphenol A, J. Mater. Chem. A 2 (22) (2014) 8534–8544. doi:10.1039/C4TA00578C.

[15] S. K. Friedlander, Chemical element balances and identification of air pollution sources, Environ. Sci. Technol. 7 (3) (1973) 235–240. doi:10.1021/es60075a005.

[16] T. Novakov, P. K. Mueller, A. E. Alcocer, J. W. Otvos, Chemical composition of Pasadena aerosol by particle size and time of day. III. Chemical states of nitrogen and sulfur by photoelectron spectroscopy, J. Colloid Interface Sci. 39 (1) (1972) 225–234. doi:10.1016/0021-9797(72)90156-7.

[17] C. Marcolli, F. Mahrt, B. Kärcher, Soot PCF: pore condensation and freezing framework for soot aggregates, Atmos. Chem. Phys. 21 (10) (2021) 7791–7843. doi:10.5194/acp-21-7791-2021.

[18] R. L. Vander Wal, A. J. Tomasek, Soot oxidation: dependence upon initial nanostructure, Combust. Flame 134 (1) (2003) 1–9. doi:10.1016/S0010-2180(03)00084-1.

[19] K. Gao, F. Friebel, C.-W. Zhou, Z. A. Kanji, Enhanced soot particle ice nucleation ability induced by aggregate compaction and densification, Atmos. Chem. Phys. 22 (7) (2022) 4985–5016. doi:10.5194/acp-22-4985-2022.

[20] D. Lizonova, A. Nagarkar, P. Demokritou, G. A. Kelesidis, Effective density of inhaled environmental and engineered nanoparticles and its impact on the lung deposition and dosimetry, Part. Fibre Toxicol. 21 (1) (2024) 1–11. doi:10.1186/s12989-024-00567-9.

[21] G. A. Kelesidis, N. Rossi, S. E. Pratsinis, Porosity and crystallinity dynamics of carbon black during internal and surface oxidation, Carbon 197 (2022) 334–340. doi:10.1016/j.carbon.2022.06.020.

[22] A. S. Pipal, H. Rohra, R. Tiwari, A. Taneja, Particle size distribution, morphometric study and mixing structure of accumulation and ultrafine aerosols emitted from indoor activities in different socioeconomic microenvironment, Atmos. Pollut. Res. 12 (4) (2021) 101–111. doi:10.1016/j.apr.2021.02.015.

[23] B. D. Zdravkov, J. J. Čermák, M. Šefara, J. Janků, Pore classification in the characterization of porous materials: A perspective, Cent. Eur. J. Chem. 5 (2) (2007) 385–395. doi:10.2478/s11532-007-0017-9.

[24] J. Rouquerol, D. Avnir, C. W. Fairbridge, D. H. Everett, J. M. Haynes, N. Pernicone, J. D. F. Ramsay, K. S. W. Sing, K. K. Unger, Recommendations for the characterization of porous solids (Technical Report), Pure Appl. Chem. 66 (8) (1994) 1739–1758. doi:10.1351/pac199466081739.

[25] J. Choma, J. Jagiello, M. Jaroniec, Assessing the contribution of mi-

779 cropores and mesopores from nitrogen adsorption on nanoporous car-
780 bons: Application to pore size analysis, Carbon 183 (2021) 150–157.
781 doi:10.1016/j.carbon.2021.07.020.

782 [26] G. Wang, Y. Ju, Organic shale micropore and mesopore structure char-
783 acterization by ultra-low pressure N2 physisorption: Experimental pro-
784 cedure and interpretation model, J. Nat. Gas Sci. Eng. 27 (2015) 452–
785 465. doi:10.1016/j.jngse.2015.08.003.

786 [27] K. J. Rockne, G. L. Taghon, D. S. Kosson, Pore structure of soot
787 deposits from several combustion sources, Chemosphere 41 (8) (2000)
788 1125–1135. doi:10.1016/S0045-6535(00)00040-0.

789 [28] T. Miyata, A. Endo, T. Ohmori, T. Akiya, M. Nakaiwa, Evaluation of
790 pore size distribution in boundary region of micropore and mesopore
791 using gas adsorption method, J. Colloid Interface Sci. 262 (1) (2003)
792 116–125. doi:10.1016/S0021-9797(02)00254-0.

793 [29] U. Mathis, M. Mohr, R. Kaegi, A. Bertola, K. Boulouchos, Influ-
794 ence of Diesel Engine Combustion Parameters on Primary Soot Par-
795 ticle Diameter, Environ. Sci. Technol. 39 (6) (2005) 1887–1892. doi:
796 10.1021/es049578p.

797 [30] H. Jiang, T. Li, Y. Wang, P. He, Morphology and nano-structure analy-
798 sis of soot particles sampled from high pressure diesel jet flames un-

der diesel-like conditions, Meas. Sci. Technol. 29 (4) (2018) 045801. doi:10.1088/1361-6501/aaa667.

[31] A. Mészáros, The number concentration and size distribution of the soot particles in the 0.02–0.5 μm radius range at sites of different pollution levels, Sci. Total Environ. 36 (1984) 283–288. doi:10.1016/0048-9697(84)90278-X.

[32] N. P. Ivleva, U. McKeon, R. Niessner, U. Pöschl, Raman Microspectroscopic Analysis of Size-Resolved Atmospheric Aerosol Particle Samples Collected with an ELPI: Soot, Humic-Like Substances, and Inorganic Compounds, Aerosol Sci. Technol. (Jun. 2007).
URL https://www.tandfonline.com/doi/full/10.1080/02786820701376391

[33] H. A. Michelsen, Probing soot formation, chemical and physical evolution, and oxidation: A review of in situ diagnostic techniques and needs, Proc. Combust. Inst. 36 (1) (2017) 717–735. doi:10.1016/j.proci.2016.08.027.

[34] T. M. Gruenberger, M. Moghiman, P. J. Bowen, N. Syred, Dynamics of soot formation by turbulent combustion and thermal decomposition of natural gas, Combust. Sci. Technol. (May 2002).
URL https://www.tandfonline.com/doi/abs/10.1080/713713038

[35] L. Pascazio, J. W. Martin, K. Bowal, J. Akroyd, M. Kraft, Exploring

the internal structure of soot particles using nanoindentation: A reactive molecular dynamics study, Combust. Flame 219 (2020) 45–56. doi:10.1016/j.combustflame.2020.04.029.

[36] K. M. Mukut, A. Ganguly, E. Goudeli, G. A. Kelesidis, S. P. Roy, Physical, chemical and morphological evolution of incipient soot obtained from molecular dynamics simulation of acetylene pyrolysis, Fuel 373 (2024) 132197. doi:10.1016/j.fuel.2024.132197.

[37] K. M. Mukut, A. Ganguly, E. Goudeli, G. A. Kelesidis, S. P. Roy, Internal Structure of Incipient Soot from Acetylene Pyrolysis Obtained via Molecular Dynamics Simulations, J. Phys. Chem. A 128 (26) (2024) 5175–5187. doi:10.1021/acs.jpca.4c01548.

[38] A. Sharma, K. M. Mukut, S. P. Roy, E. Goudeli, The coalescence of incipient soot clusters, Carbon 180 (2021) 215–225. doi:10.1016/j.carbon.2021.04.065.

[39] J. Mei, Y. Zhou, X. You, C. K. Law, Formation of nascent soot during very fuel-rich oxidation of ethylene at low temperatures, Combust. Flame 226 (2021) 31–41. doi:10.1016/j.combustflame.2020.11.031.

[40] B. Zhao, Z. Yang, Z. Li, M. V. Johnston, H. Wang, Particle size distribution function of incipient soot in laminar premixed ethylene flames: effect of flame temperature, Proc. Combust. Inst. 30 (1) (2005) 1441–1448. doi:10.1016/j.proci.2004.08.104.

[41] M. Zhang, B. Zhou, Y. Chen, H. Gong, Kinetic Mechanism for Simulating the Temperature and Pressure Effect on the Explosive Decomposition of Acetylene by ReaxFF Molecular Dynamics, ChemistrySelect 8 (10) (2023) e202204563. doi:10.1002/slct.202204563.

[42] J. H. Kiefer, W. A. Von Drasek, W. A. Von Drasek, The mechanism of the homogeneous pyrolysis of acetylene, Int. J. Chem. Kinet. 22 (7) (1990) 747–786. doi:10.1002/kin.550220710.

[43] A. P. Thompson, H. M. Aktulga, R. Berger, D. S. Bolintineanu, W. M. Brown, P. S. Crozier, P. J. In 't Veld, A. Kohlmeyer, S. G. Moore, T. D. Nguyen, R. Shan, M. J. Stevens, J. Tranchida, C. Trott, S. J. Plimpton, LAMMPS - a flexible simulation tool for particle-based materials modeling at the atomic, meso, and continuum scales, Comput. Phys. Commun. 271 (2022) 108171. doi:10.1016/j.cpc.2021.108171.

[44] A. C. T. van Duin, S. Dasgupta, F. Lorant, W. A. Goddard, ReaxFF: A Reactive Force Field for Hydrocarbons, J. Phys. Chem. A 105 (41) (2001) 9396–9409. doi:10.1021/jp004368u.

[45] F. Castro-Marcano, A. M. Kamat, M. F. Russo, A. C. T. van Duin, J. P. Mathews, Combustion of an Illinois No. 6 coal char simulated using an atomistic char representation and the ReaxFF reactive force field, Combust. Flame 159 (3) (2012) 1272–1285. doi:10.1016/j.combustflame.2011.10.022.

[46] X. Rong, J. Shi, W. Wei, H. Jin, Reactive molecular dynamics simulations of poly(vinyl alcohol) gasification in supercritical carbon dioxide, Fuel 378 (2024) 132858. doi:10.1016/j.fuel.2024.132858.

[47] W. C. Swope, H. C. Andersen, P. H. Berens, K. R. Wilson, A computer simulation method for the calculation of equilibrium constants for the formation of physical clusters of molecules: Application to small water clusters, J. Chem. Phys. 76 (1) (1982) 637–649. doi:10.1063/1.442716.

[48] D. J. Evans, B. L. Holian, The Nose–Hoover thermostat, J. Chem. Phys. 83 (8) (1985) 4069–4074. doi:10.1063/1.449071.

[49] K. M. Mukut, S. Roy, E. Goudeli, Molecular arrangement and fringe identification and analysis from molecular dynamics (MAFIA-MD): A tool for analyzing the molecular structures formed during reactive molecular dynamics simulation of hydrocarbons, Comput. Phys. Commun. 276 (2022) 108325. doi:10.1016/j.cpc.2022.108325.

[50] J. B. Maglic, R. Lavendomme, MoloVol: an easy-to-use program for analyzing cavities, volumes and surface areas of chemical structures, J. Appl. Crystallogr. 55 (4) (2022) 1033–1044. doi:10.1107/S1600576722004988.

[51] L. Schrödinger, W. DeLano, Pymol.
URL http://www.pymol.org/pymol

[52] StereoFractAnalyzer, [Online; accessed 3. Oct. 2024] (Oct. 2024).
URL https://github.com/comp-comb/StereoFractAnalyzer

[53] L. van der Maaten, G. Hinton, Visualizing Data using t-SNE, Journal of Machine Learning Research 9 (86) (2008) 2579–2605.
URL https://www.jmlr.org/papers/v9/vandermaaten08a.html

[54] S. Lloyd, Least squares quantization in PCM, IEEE Trans. Inf. Theory 28 (2) (1982) 129–137. doi:10.1109/TIT.1982.1056489.

[55] K. Chenoweth, A. C. T. van Duin, W. A. Goddard, ReaxFF Reactive Force Field for Molecular Dynamics Simulations of Hydrocarbon Oxidation, J. Phys. Chem. A 112 (5) (2008) 1040–1053. doi:10.1021/jp709896w.

[56] C. Ashraf, A. C. T. van Duin, Extension of the ReaxFF Combustion Force Field toward Syngas Combustion and Initial Oxidation Kinetics, J. Phys. Chem. A 121 (5) (2017) 1051–1068. doi:10.1021/acs.jpca.6b12429.

[57] Q. Mao, A. C. T. van Duin, K. H. Luo, Formation of incipient soot particles from polycyclic aromatic hydrocarbons: A ReaxFF molecular dynamics study, Carbon 121 (2017) 380–388. doi:10.1016/j.carbon.2017.06.009.

[58] S. Alvarez, A cartography of the van der Waals territories, Dalton Trans. 42 (24) (2013) 8617–8636. doi:10.1039/C3DT50599E.

[59] M. F. Sanner, A. J. Olson, J.-C. Spehner, Reduced surface: An efficient way to compute molecular surfaces, Biopolymers 38 (3) (1996) 305–320. doi:10.1002/(SICI)1097-0282(199603)38:3<305::AID-BIP4>3.0.CO;2-Y.

[60] A. Giorgilli, D. Casati, L. Sironi, L. Galgani, An efficient procedure to compute fractal dimensions by box counting, Phys. Lett. A 115 (5) (1986) 202–206. doi:10.1016/0375-9601(86)90465-2.

[61] R. Wang, A. K. Singh, S. R. Kolan, E. Tsotsas, Fractal analysis of aggregates: Correlation between the 2D and 3D box-counting fractal dimension and power law fractal dimension, Chaos, Solitons Fractals 160 (2022) 112246. doi:10.1016/j.chaos.2022.112246.

[62] M. Shelberg, N. Lam, H. Moellering, Measuring the fractal dimension of surfaces, Tech. rep., [Online; accessed 5. Oct. 2024] (1983).
URL https://apps.dtic.mil/sti/tr/pdf/ADA129664.pdf

[63] K. C. Clarke, Computation of the fractal dimension of topographic surfaces using the triangular prism surface area method, Comput. Geosci. 12 (5) (1986) 713–722. doi:10.1016/0098-3004(86)90047-6.

[64] D. K. Lee, J. In, S. Lee, Standard deviation and standard error of the mean, Korean Journal of Anesthesiology 68 (3) (2015) 220. doi:10.4097/kjae.2015.68.3.220.

[65] M. Frenklach, Reaction mechanism of soot formation in flames, Phys. Chem. Chem. Phys. 4 (11) (2002) 2028–2037. doi:10.1039/B110045A.

[66] K. M. Leung, R. P. Lindstedt, W. P. Jones, A simplified reaction mechanism for soot formation in nonpremixed flames, Combust. Flame 87 (3) (1991) 289–305. doi:10.1016/0010-2180(91)90114-Q.

[67] F. Schulz, M. Commodo, K. Kaiser, G. De Falco, P. Minutolo, G. Meyer, A. D`anna, L. Gross, Insights into incipient soot formation by atomic force microscopy, Proc. Combust. Inst. 37 (1) (2019) 885–892. doi:10.1016/j.proci.2018.06.100.

[68] P. D. Teini, D. M. A. Karwat, A. Atreya, Observations of nascent soot: Molecular deposition and particle morphology, Combust. Flame 158 (10) (2011) 2045–2055. doi:10.1016/j.combustflame.2011.03.005.

[69] M. L. Botero, D. Chen, S. González-Calera, D. Jefferson, M. Kraft, HRTEM evaluation of soot particles produced by the non-premixed combustion of liquid fuels, Carbon 96 (2016) 459–473. doi:10.1016/j.carbon.2015.09.077.

[70] J. Camacho, Y. Tao, H. Wang, Kinetics of nascent soot oxidation by molecular oxygen in a flow reactor, Proc. Combust. Inst. 35 (2) (2015) 1887–1894. doi:10.1016/j.proci.2014.05.095.

[71] G. A. Kelesidis, S. E. Pratsinis, Estimating the internal and surface

oxidation of soot agglomerates, Combust. Flame 209 (2019) 493–499. doi:10.1016/j.combustflame.2019.08.001.

[72] A. Violi, Modeling of soot particle inception in aromatic and aliphatic premixed flames, Combust. Flame 139 (4) (2004) 279–287. doi:10.1016/j.combustflame.2004.08.013.

[73] M. Schenk, S. Lieb, H. Vieker, A. Beyer, A. Gölzhäuser, H. Wang, K. Kohse-Höinghaus, Morphology of nascent soot in ethylene flames, Proc. Combust. Inst. 35 (2) (2015) 1879–1886. doi:10.1016/j.proci.2014.05.009.

[74] J. R. Grace, A. Ebneyamini, Connecting particle sphericity and circularity, Particuology 54 (2021) 1–4. doi:10.1016/j.partic.2020.09.006.

[75] Q. Song, B. He, Q. Yao, Z. Meng, C. Chen, Influence of Diffusion on Thermogravimetric Analysis of Carbon Black Oxidation, Energy Fuels 20 (5) (2006) 1895–1900. doi:10.1021/ef0600659.

[76] F.-X. Ouf, S. Bourrous, C. Vallières, J. Yon, L. Lintis, Specific surface area of combustion emitted particles: Impact of primary particle diameter and organic content, J. Aerosol Sci. 137 (2019) 105436. doi:10.1016/j.jaerosci.2019.105436.

[77] J. Sun, J. Niu, M. Liu, J. Ji, M. Dou, F. Wang, Biomass-derived nitrogen-doped porous carbons with tailored hierarchical porosity and

high specific surface area for high energy and power density supercapacitors, Appl. Surf. Sci. 427 (2018) 807–813. doi:10.1016/j.apsusc.2017.07.220.

[78] D. Kang, Q. Liu, J. Gu, Y. Su, W. Zhang, D. Zhang, "Egg-Box"-Assisted Fabrication of Porous Carbon with Small Mesopores for High-Rate Electric Double Layer Capacitors, ACS Nano 9 (11) (2015) 11225–11233. doi:10.1021/acsnano.5b04821.

[79] J.-S. M. Lee, M. E. Briggs, T. Hasell, A. I. Cooper, Hyperporous Carbons from Hypercrosslinked Polymers, Adv. Mater. 28 (44) (2016) 9804–9810. doi:10.1002/adma.201603051.

[80] C. M. Sorensen, Light Scattering by Fractal Aggregates: A Review, Aerosol Sci. Technol. (Jan. 2001).
URL https://www.tandfonline.com/doi/abs/10.1080/02786820117868

[81] D. Avnir, D. Farin, P. Pfeifer, Molecular fractal surfaces, Nature 308 (1984) 261–263. doi:10.1038/308261a0.

[82] D. Avnir, D. Farin, P. Pfeifer, Chemistry in noninteger dimensions between two and three. II. Fractal surfaces of adsorbents, J. Chem. Phys. 79 (7) (1983) 3566–3571. doi:10.1063/1.446211.

[83] C. Ahl, J. Niemeyer, The fractal dimension of the pore-volume inside

soils, Z. Pflanzenernähr. Bodenkd. 152 (5) (1989) 457–458. doi:10.1002/jpln.19891520512.

[84] H. P. Tang, J. Z. Wang, J. L. Zhu, Q. B. Ao, J. Y. Wang, B. J. Yang, Y. N. Li, Fractal dimension of pore-structure of porous metal materials made by stainless steel powder, Powder Technol. 217 (2012) 383–387. doi:10.1016/j.powtec.2011.10.053.

[85] A. W. Kandas, I. Gokhan Senel, Y. Levendis, A. F. Sarofim, Soot surface area evolution during air oxidation as evaluated by small angle X-ray scattering and CO2 adsorption, Carbon 43 (2) (2005) 241–251. doi:10.1016/j.carbon.2004.08.028.

[86] F. Ehrburger-Dolle, M. Holz, J. Lahaye, Use of N2, Ar and CO2 adsorption for the determination of microporosity and surface fractal dimension of carbon blacks and silicas, Pure Appl. Chem. 65 (10) (1993) 2223–2230. doi:10.1351/pac199365102223.

[87] G. A. Kelesidis, P. Crepaldi, S. E. Pratsinis, Oxidation dynamics of soot or carbon black accounting for its core-shell structure and pore network, Carbon 219 (2024) 118764. doi:10.1016/j.carbon.2023.118764.

[88] V. Hegedűs, F. Kerényi, R. Boda, D. Horváth, I. Lázár, E. Tóth-Győri, B. Dezső, C. Hegedus, β-Tricalcium phosphate-silica aerogel as an alternative bioactive ceramic for the potential use in dentistry, Adv.

Appl. Ceram. 119 (5-6) (2020) 364–371. doi:10.1080/17436753.2019.1625567.

[89] H. Demiral, İ. Demiral, Preparation and characterization of carbon molecular sieves from chestnut shell by chemical vapor deposition, Adv. Powder Technol. 29 (12) (2018) 3033–3039. doi:10.1016/j.apt.2018.07.015.

[90] M. Frenklach, H. Wang, Detailed modeling of soot particle nucleation and growth, Symp. Combust. 23 (1) (1991) 1559–1566. doi:10.1016/S0082-0784(06)80426-1.

[91] G. A. Kelesidis, A. Nagarkar, P. G. Rivano, Solar steam generation enabled by carbon black: The impact of particle size and nanostructure, AIChE J. 70 (12) (2024) e18619. doi:10.1002/aic.18619.

[92] S. Khodabakhshi, P. F. Fulvio, E. Andreoli, Carbon black reborn: Structure and chemistry for renewable energy harnessing, Carbon 162 (2020) 604–649. doi:10.1016/j.carbon.2020.02.058.

Appendix A. List of Symbols and Definitions

Table A.1: List of symbols and their definitions used in the main text.

Symbol	Definition	Scope	Equation No.
Ψ	Sphericity of an incipient particle	Particle	B.1
ψ	Sphericity of a single pore (cavity)	Cavity	B.6
Φ	Porosity of an incipient particle	Particle	B.4
σ	Circularity of an incipient particle	Particle	B.2
D_S	Surface fractal dimension of an incipient particle	Particle	
D_V	Volume fractal dimension of an incipient particle	Particle	
D_f	Aggregate fractal dimension of a soot aggregate	N/A	
A_p	Total pore surface area ($Å^2$) within a particle	Particle	1
V_p	Total pore volume ($Å^3$) in a particle	Particle	1, B.4
A_{Ext}	External surface area ($Å^2$) of a particle	Particle	B.1
A_{pi}	Surface area of the i^{th} pore ($Å^2$)	Cavity	3
V_{pi}	Volume of the i^{th} pore ($Å^3$)	Cavity	3
V	Material volume of an incipient particle ($Å^3$)	Particle	2
V_B	Bulk volume of the particle ($Å^3$) including void volume (i.e., $V + V_p$)	Particle	B.1, B.4
ρ_b	Bulk density (g/cm^3) of an incipient particle (calculated using bulk volume and mass of a particle)	Particle	B.5
d_V	Volume-equivalent diameter (Å) of an incipient particle (based on bulk volume)	Particle	B.5
$SSA_{Theoretical}$	Theoretical specific surface area (m^2/g) of an incipient particle	Particle	B.5
D_{SC}	Surface fractal dimension of a cavity	Cavity	
D_{VC}	Volume fractal dimension of a cavity	Cavity	
$\bar{\psi}_{Tunnel}$	Average pore sphericity for tunnel cavities in an ensemble of incipient particles	Ensemble	B.6
$\bar{\psi}_{Pocket}$	Average pore sphericity for pocket cavities in an ensemble of incipient particles	Ensemble	B.6
$\bar{\psi}_{Isolated}$	Average pore sphericity for isolated cavities in an ensemble of incipient particles	Ensemble	B.6
d_p	Volume-equivalent diameter of a cavity (Å)	Cavity	B.7
$V_C(d_p)$	Cumulative void volume per unit mass (cm^3/g) within an incipient particle up to cavity size d_p	Particle	B.7
$\overline{d_p}$	Average volume-equivalent diameter of cavities within an incipient particle	Particle	

Appendix B. Mathematical Equations

Below is the collection of equations used throughout the manuscript, arranged in the order they are discussed in the main text.

Sphericity (Ψ, dimensionless) is calculated using

$$\Psi = \frac{\pi^{1/3}(6 \times V_B)^{2/3}}{A_{Ext}} \tag{B.1}$$

where V_B is the bulk volume of the particle (Å^3), and A_{Ext} is the external surface area (Å^2).

Circularity (σ, dimensionless) and average circularity ($\bar{\sigma}$, dimensionless) are calculated as

$$\sigma = \frac{P_c}{P} \tag{B.2}$$

$$\bar{\sigma} = \frac{1}{N} \sum_{i=1}^{N} \left(\frac{P_c}{P} \right)_i, \quad N = 10 \tag{B.3}$$

where P_c is the perimeter of a circle of the same projected area, P is the actual perimeter of the projected area. Average circularity is calculated over 10 projections.

Porosity (Φ, dimensionless) is calculated using

$$\Phi = \frac{V_p}{V_B} \tag{B.4}$$

where V_p is the total pore volume (Å^3), and V_B is the bulk volume of the particle (Å^3).

Theretical specific surface area ($\text{SSA}_{Theoretical}$, m^2/g) is evaluated using

$$\begin{aligned} SSA_{\text{Theoretical}} &= \frac{\text{Surface area}}{\text{Bulk Volume } \times \text{Bulk Density}} \\ &= \frac{\pi {d_V}^2}{\frac{1}{6}\pi {d_V}^3 \times \rho_b} \\ &= \frac{6}{d_V \times \rho_b} \end{aligned} \tag{B.5}$$

where d_V is the volume-equivalent diameter (Å), and ρ_b is the bulk density (g/cm^3).

Average pore sphericity ($\bar{\psi}$, dimensionless) for different types of pores are calculated using

$$\bar{\psi} = \frac{1}{N_{particles}} \sum_{i}^{N_{particles}} \frac{1}{n_i} \sum_{j}^{n_i} \psi_j \tag{B.6}$$

where $N_{particles}$ is the total number of particles, n_i is the number of cavities in particle i, and ψ_j is the sphericity of the j^{th} cavity in particle i.

Cumulative void volume per unit mass ($V_C(d_p)$, cm^3/g) is caculated using

$$V_C(d_p) = \sum_{i}^{N_{particle}} \frac{1}{M_i} \sum_{j}^{n_i} v_{c,j} \mathcal{H}(d_{p,j} - d_p) \tag{B.7}$$

where M_i is mass of particle i, and $\mathcal{H}$ is the Heaviside step function, and d_p represents the pore size.